Preprint

Final Version can be found here:
http://dx.doi.org/10.1016/j.isprsjprs.2015.03.003

Comparative classification analysis of post-harvest growth detection from terrestrial LiDAR point clouds in precision agriculture

Kristina Koenig[a], Bernhard Höfle[a], Martin Hämmerle[a], Thomas Jarmer[b], Bastian Siegmann[b], Holger Lilienthal[c]

[a] Institute of Geography, Heidelberg University, Germany
[b] Institute for Geoinformatics and Remote Sensing, University of Osnabrueck, Germany
[c] Julius-Kühn-Institut (JKI), Institute for Crop and Soil Science, Braunschweig, Germany

Abstract

In precision agriculture, detailed geoinformation on plant and soil properties plays an important role, e.g., in crop protection or the application of fertilizers. This paper presents a comparative classification analysis for post-harvest growth detection using geometric and radiometric point cloud features of terrestrial laser scanning (TLS) data, considering the local neighborhood of each point. Radiometric correction of the TLS data was performed via an empirical range-correction function derived from a field experiment. Thereafter, the corrected amplitude and local elevation features were explored regarding their importance for classification. For the comparison, tree induction, Naïve Bayes, and *k*-Means-derived classifiers were tested for different point densities to distinguish between ground and post-harvest growth. The classification performance was validated against highly detailed RGB reference images and the red edge normalized difference vegetation index ($NDVI_{705}$), derived from a hyperspectral sensor. Using both geometric and radiometric features, we achieved a precision of 99% with the tree induction. Compared to the reference image classification, the calculated post-harvest growth coverage map reached an accuracy of 80%. RGB and LiDAR-derived coverage showed a polynomial correlation to $NDVI_{705}$ of degree two with R^2 of 0.8 and 0.7, respectively. Larger post-harvest growth patches (> 10 x 10 cm) could already be detected by a point density of 2 pts. / 0.01 m². The results indicate a high potential of radiometric and geometric LiDAR point cloud features for the identification of post-harvest growth using tree induction classification. The proposed technique can potentially be applied over larger areas using vehicle-mounted scanners.

Keywords

Terrestrial Laser Scanning; Radiometric Correction; Radiometric Feature; Geometric Feature; Classification; Precision Agriculture

1. Introduction

1.1. Importance of Post-Harvest Growth Management

Detection and control of post-harvest growth (weed and second growth) are important fields of precision agriculture (PA) (Weis et al., 2008). In most crops, post-harvest growth negatively influences yields because of the additional competition for nutrients, water, and light, or due to insects and diseases settling down within post-harvest growth (Zimdahl, 2013). In case of second growth, such problems are due to seeds of low quality, which fall to the ground as a result of bad weather conditions and delayed harvest, or due to the cultivation of transgenic crops in combination with less tillage. Depending on the crop, seeds can be germinable for many years and influence the growing crops. Although these effects and the countermeasures depend strongly on crop and weed species, lower crop quantity and quality occur in general if post-harvest growth is not controlled. Common measures for weed control are the extensive pre- and post-emergent application of chemicals (Thorp & Tian, 2004). On the one hand extensive use of pesticides reduces the weed appearance, on the other hand it has negative direct and indirect effects on the ecosystem such as reduced soil quality or water pollution (Arias-Estévez et al., 2008; Smith et al., 2011). Apart from the ecological aspects, farmers have to stick to standardized environmental regulations and laws such as the European Water Framework Directive (WFD) (2000/60EG) or regulations of cross-compliance. In European countries the usage of pesticides is strictly regulated to minimize negative environmental effects. For example, the German law (§12 f. IV PflSchG) prescribes the use of economic weed thresholds based on plants per square meter at which control is economically justified. Such thresholds provide valuable decision aids for weed control, indicating at which weed density pesticides need to be applied (Weis et al., 2008). However, these thresholds discount the nature of weeds growing in patches (Lamb & Brown, 2001). The most effective means of weed control are prevention (control prior to planting), early detection (within the first stages of growth) and eradication (Christensen et al., 2009). The concept of site-specific weed management (SSWM) in precision farming thus plays an important role in reducing the negative environmental effects of weed control. At the same time it can improve the efficiency of growing crops (Christensen et al., 2009).

1.2. Methods for Site-Specific Management and Mapping

Crop and field management in PA apply techniques and methods gathering site-specific information. Site-specific information is geo-referenced information of spatially distributed environmental factors and their heterogeneity and variability (soil properties, nutrients, plant diseases or weed emergence) (Torres-Sánchez et al., 2013). Such information serves as a basis for precisely located weed control applications (Heege, 2013). Within weed management, accurate herbicide application requires a precise detection and positioning of weeds. Mapping of weeds can be done manually by recognizing weed species in the field or indirectly by remote sensing of total plant coverage, leaf area index, and photosynthetic activity or plant height with sensors located on ground vehicles (Peteinatos et al., 2014). A series of optoelectronic, imaging, or distance sensors have been widely applied in agricultural studies (Mulla, 2013; Vibhute

& Gawali, 2013) for mapping the environmental factors such as chemical soil properties (Anderson, 2009; Jarmer et al., 2008; Palacios-Orueta & Ustin, 1998) and plant water content (Meron et al., 2010), as well as for capturing crop conditions (Jarmer, 2013; Lumme et al., 2008 , Tilly et al., 2014) and weed distribution (Andújar et al., 2013; Lamb & Brown, 2001; Torres-Sánchez et al., 2013). Based on the selective spectral absorption, different indices such as the normalized differenced vegetation index (NDVI (Feyaerts & Gool, 2001)), the excess green index (ExG (Sena et al., 2011)) or the vegetative index (VI, (Hague, 2006)) are usually calculated to separate soil and plants (Peteinatos et al., 2014) for weed detection. Optical sensors are often combined with an herbicide sprayer, which is automatically turned on when the used index exceeds a specific threshold. However, the integrated value of plant and soil coverage for the whole field of view limits the spatial information and thus the detection of smaller weed patches. Further loss in classification accuracy is due to influencing factors such as changing ambient light conditions in the field and the need of rectification or repeated calibration in the field (Peteinatos et al., 2014). Weed detection can also be done by means of image processing methods, using infrared, multispectral, or RGB cameras to extract plant properties (Andújar et al., 2011; Gerhards & Oebel, 2006; Romeo et al., 2013; Weis & Gerhards, 2007) employing color, shape, and texture features (Guijarro et al., 2011; McCarthy et al., 2010; Pérez et al., 2000; Rumpf et al., 2012; Tellaeche et al., 2011), either taken from a low distance above ground mounted on agricultural vehicles or by Unmanned Aerial Vehicles (UAV) based remote sensing (Peña et al., 2013; Primicerio et al., 2012; Torres-Sánchez et al., 2013; Zhang & Kovacs, 2012).

Imaging sensors are able to provide significant results concerning the location of weeds and crops, but they disregard 3D geometric information like plant height. However, height is an important parameter for estimating the amount of herbicide, considering the biomass of weeds or second growths.

1.3. LiDAR for Vegetation Analysis and Agricultural Applications

Light detection and ranging (LiDAR), also referred to as laser scanning (LS), has evolved into a state-of-the-art technology for highly accurate 3D data acquisition. Airborne as well as ground-based systems are used to capture information about agricultural objects, however most recent studies use terrestrial laser scanning (TLS). Compared to airborne LS, the major advantages of TLS are a low-cost operation, easier multitemporal data acquisition, and high-density point clouds (multiple points per cm² possible). LiDAR technology enables a detailed geometric (high-resolution XYZ point clouds and derived parameters, e.g., object height) and radiometric (e.g., strength of backscatter (Höfle & Pfeifer, 2007)) representation of the scanned object. Several studies have already indicated the potential of LS in vegetation description, for example in tree (Rosell & Sanz, 2012; Rosell et al., 2009; Sanz-Cortiella et al., 2011;) or grain crop monitoring (Höfle, 2014; Llorens et al., 2011; Lumme et al., 2008; Saeys et al., 2009) with a stationary or tractor-mounted scanner. Until now, LiDAR sensors in agricultural applications are mainly used for gathering the geometric information for, e.g., estimating crop height for biomass calculation or for growth monitoring (Ehlert et al., 2009; Hoffmeister et al., 2010; Hosoi & Omasa, 2009; Tilly et al., 2014; Zhang & Grift, 2012;). Radiometric information has so far rarely been used due to calibration issues, but in

recent years this information has been increasingly applied for object detection (Höfle & Hollaus, 2010; Rutzinger et al., 2008). Its application in an agricultural context is still rare. Andújar *et al.* (2013) used LiDAR height and reflection measurements for vegetation detection captured at 905 nm wavelength with a detection rate of 77.7% for *S. halepense*. Similar results are demonstrated by Koenig *et al.* (2013) and Höfle (2014) using height differences in combination with the amplitude in spatial context to distinguish soil and plant objects.

1.4. Hypotheses and Objectives

From this overview we hypothesize (i) that TLS can be used for post-harvest growth detection and discrimination and (ii) that for a complete and correct detection of post-harvest growth patches in TLS data, a combined use of geometric and radiometric information in a local neighbourhood will lead to better results, compared to a sole use of geometric information. In order to verify this hypotheses, the following objectives are addressed: (i) to evaluate the accuracy and performance of TLS for post-harvest growth detection; (ii) to assess the possibilities of radiometric information to discriminate post-harvest growth from soil; and (iii) to evaluate the effect of point density on post-harvest growth detection. The objectives were examined by applying correlation analysis and different classification methods of derived geometric and radiometric information of TLS data.

2. Study site and Datasets

The study was conducted with data from a harvested and grubbed winter barley plot (about 7 m x 66 m) with second growth of winter barley and sparsely spread weed of unknown species at the Julius-Kühn-Institut for Crop and Soil Science (JKI), Brunswick, Germany (52.288N, 10.434E). The survey was performed on 27th of August 2013 two weeks after grubbing and four weeks after harvesting. Within the investigated crop field, two reference sample plots (1 m x 1 m) were captured for training and testing the developed methods.

2.1. Terrestrial Laser Scanning Data

A time-of-flight scanner Riegl VZ-400 with full-waveform online echo detection was used to collect data from six elevated scan positions (scanner height above ground ~4 m) located around the field (Fig. 1). The laser scanner has a near-infrared laser beam (1550 nm) with a beam divergence of 0.3 mrad and a range accuracy of 5 mm at 100 m according to the manufacturer's datasheet (Riegl, Datasheet VZ-400). A nominal point spacing of 5 mm at 10 m distance was chosen for four scans and 3 mm nominal spacing for two scans for analysis regarding the point density. The study area was covered by a mean density of 28 points per 0.01 m², resulting in a point cloud of about 10.8 x 10^6 points in total.

Co-registration of scan positions was performed using tie points (cylindric reflectors) with high reflectance and six plane surface patches (e. g. EUR-palett) placed around the field. Following the initial alignment of the scans, the fine registration by the iterative closest point (ICP) algorithm integrated into the RiSCAN PRO software results

in a 0.0143 m standard deviation of error distribution between the scans. To guarantee lowest alignment errors, only points with range <30 m were chosen for the analysis. After the co-registration of the single scan positions, the point cloud was exported into an ASCII file containing the XYZ coordinates, range [m] and signal amplitude [digital number DN] for each laser point. The signal amplitude was rescaled to [0,1] based on the known reflectance of a reference target which was captured with every scan. The reference target (20 x 20 cm) was made of Spectralon® with Lambertian scattering properties. At the scanner's operating wavelength of 1550 nm, the nominal reflectance of the target was 92.5%. The target was mounted on a tripod, its center was oriented to the scanner, and the distance from target to scanner differed with each scan position.

Within the investigated field, training data was manually extracted from the point cloud and further refined by visual comparison to the RGB images. The training data consists of several small samples of ground and post-harvest growth data and was used in the feature calculation, the correlation analysis, and the model construction.

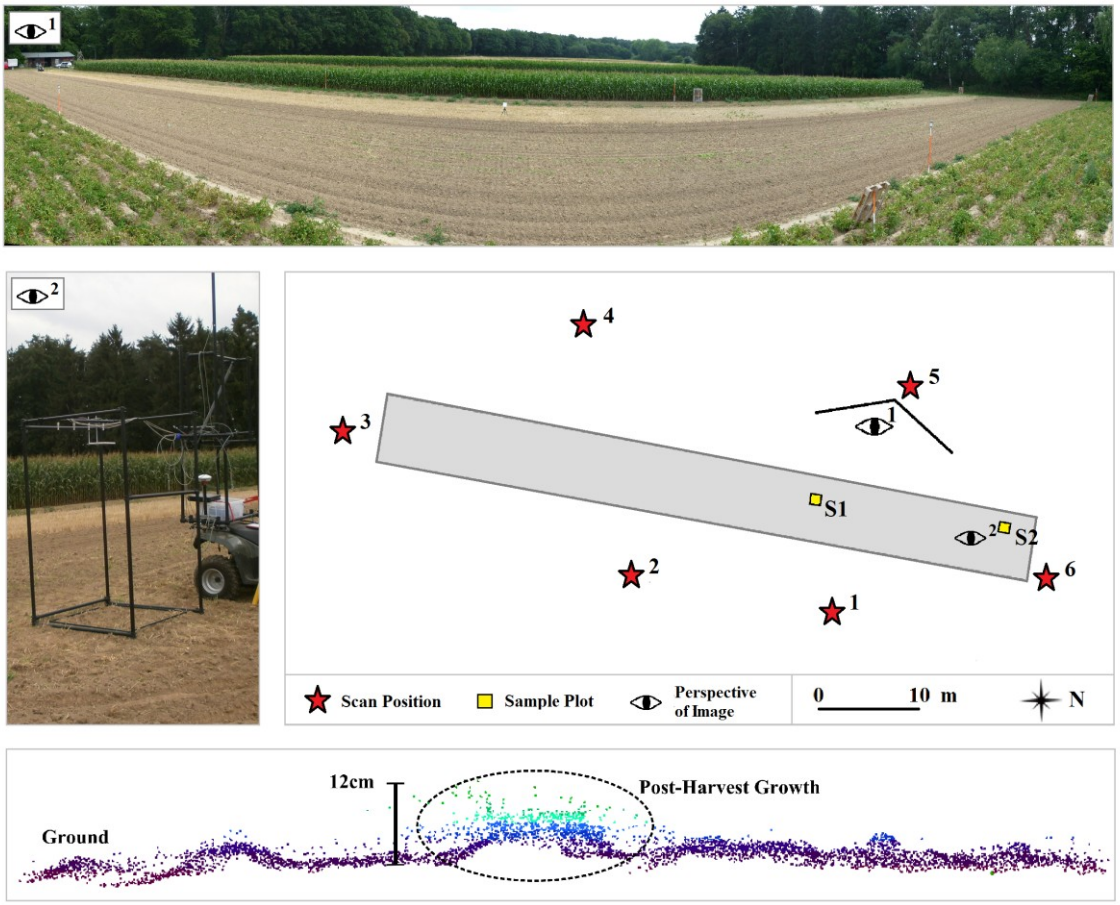

Fig. 1. Study area, covering a harvested and grubbed winter barley field with patches of post-harvest growth of winter barley. Scan positions and location of the two sample plots are given as well as an elevation profile within the field showing points of post-harvest growth and ground, colored by elevation. Perspective 1: panorama at scan position 5; Perspective 2: measuring setup for the acquisition of RGB images and hyperspectral data at the two sample plots.

2.2. Reference Data

The point cloud based classification results were validated with 1) an independent classification of the 1 m² reference plots done by image analysis of high-resolution RGB photographs and 2) by the $NDVI_{705}$ calculated from hyperspectral data. The RGB image post-harvest growth detection was based on georeferenced binary images of one square meter and was realized using a decision tree (DT) with one rule node. The images were acquired perpendicular from a height of 1.5 m, with a ground resolution of 0.05 mm. Two threshold values (one for the red and one for the blue band of the RGB image) were used to classify the image with two classes: 'ground' and 'post-harvest growth'. The accuracy assessment of RGB image classification was based on stratified random sampling of 256 points from the classified image, with at least 100 points per class, and the manual comparison of them with the original RGB image. The RGB image classification achieved an overall accuracy of 94.9%. The hyperspectral data of the whole field was captured with the Penta-Spek system developed by the JKI (Lilienthal et al., 2012; Lilienthal & Schnug, 2010). Compared to airborne acquisition, atmospheric and geometric corrections were negligible due to the proximity of sensor and ground. The system comprised five hyperspectral sensors (Ocean Optics Inc.) with an effective resolution of 46 channels at 10 nm and a minimal detection time of 3 msec. Four sensors were oriented groundwards and one skywards to measure the irradiation reference and to correct the sensors. Thus, the spectral reflections could be directly determined in the field. All sensors covered the same spectral range of 400 nm to 925 nm. The four sensors were mounted row-wise 25 cm apart from each other and 2 m above the ground on a frame, each having a ground resolution of 25 cm. $NDVI_{705}$ was calculated for each sensor and resulted in 16 measuring points. The two reference datasets were co-registered to the point cloud via corresponding point pairs.

3. Methods

The developed workflow (Fig. 2) was based on the assumption that post-harvest growth is characterized by: 1) a defined vertical extent (height above ground) and a variation of local neighboring points (geometric criteria); and 2) differing amplitudes of post-harvest growth and ground (radiometric criteria). Here, the category 'ground' comprised bare soil and dry straw of winter barley lying on the ground, whereas weed and second growth of winter barley constituted the category 'post-harvest growth'.

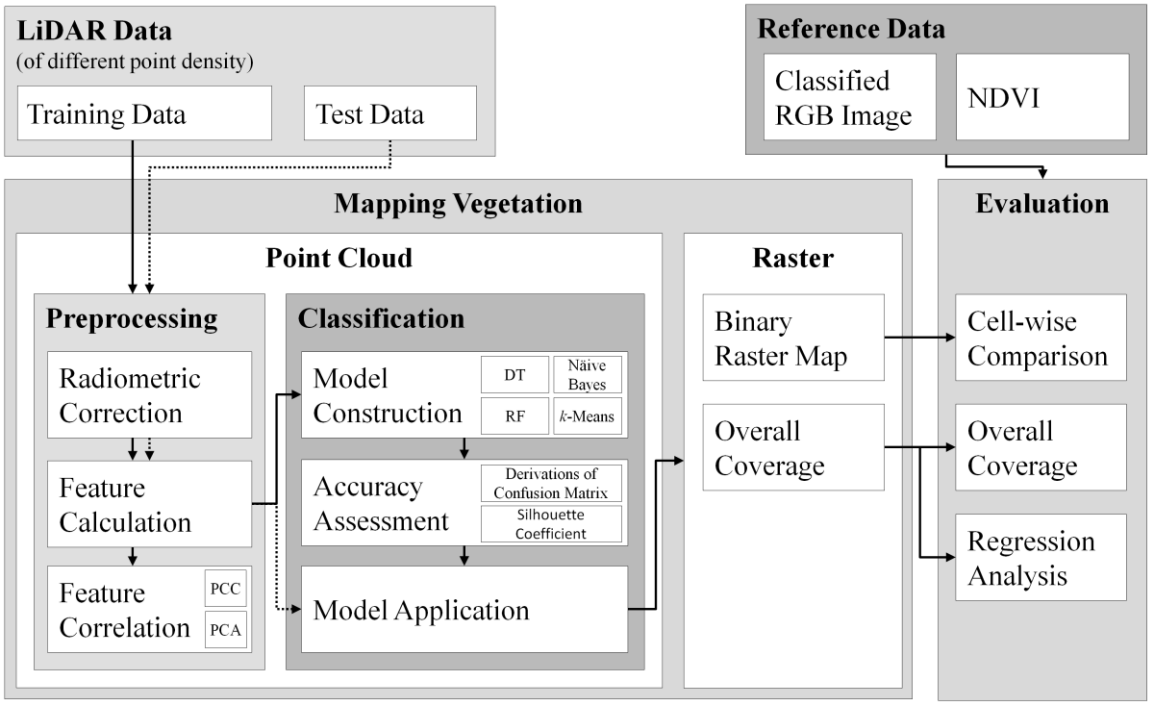

Fig. 2. Workflow for mapping 'post-harvest growth' by using full-waveform point clouds of varying point density. After preprocessing of radiometric correction and feature calculation within a local neighborhood for the whole data, four different approaches of classification and model construction were applied to training data. The derived models were evaluated by assigning to test data and by using the classified RGB image and $NDVI_{705}$ derived from hyperspectral data.

3.1. Data Preprocessing

3.1.1. Data Cleaning: Radiometric Correction

Data cleaning attempts to identify and remove outliers in order to correct inconsistencies in the data. Apart from geometric features (XYZ coordinates) the laser scanner gathers radiometric features (e.g. signal amplitude) from all scanned surfaces. The recorded signal is affected by the scanning geometry, the target properties, and atmospheric and sensor settings and parameters (Höfle, 2014; Kaasalainen et al., 2011). Scanning geometry is described by range (distance) and incoming beam incidence angle to the target (Kaasalainen et al., 2011), which influences the backscattered signal. For TLS, the distance effect seems to depend mostly on the instrument (detector effects or receiver optics) (Höfle, 2014; Pfeifer et al., 2008) and not entirely following the $1/R^2$ law of the radar equation in near distances (< 20 m for Riegl VZ-400) as mostly valid for ALS (Wagner, 2010). In our case, radiometric correction aimed at removal of the range effect.

First, vertical outliers in the point cloud were removed manually. A data-driven range correction approach was applied by estimating the range-amplitude function $f(r)$ and the resulting correction factor $1/f(r)$ for multiplying the recorded values from field data (Höfle, 2014). The selected reference surface consists of a homogeneous 0.8 x 40.0 m subset of one scan position covering dry and bare soil. Due to artificially managed and well understood soil conditions and mechanized harvesting, this area was considered sufficiently homogeneous to serve as a reference. A moving median filter of

amplitude with a 0.3 m overlap in range was applied to suppress small scale variations, e.g. due to surface roughness. Polynomial functions from degree 1 to 14 were tested as models for the radiometric correction. The correction function *f(r)* results from the Least-Squares (LSQ) fitting of polynomial functions with the lowest root-mean-square error (RMSE).

In order to evaluate the performance of the range correction, the same reference target of 20 cm x 20 cm with known reflectance (Spectralon®) was placed in each scan position, but always at a different distance from the scanner (from 16 m to 24 m). By using the identical Spectralon target with known and constant reflectance, the corrected amplitude values should be similar for all LiDAR points on the target in each scan. The median amplitude was calculated for each target. Subsequently the standard deviation (in percentage) of all target medians was assessed as a measure of success of the radiometric correction. Thus, the standard deviation of all medians should be decreased strongly after the range correction, thus indicating the removal of the distance effect.

3.1.2. Feature Calculation

Based on the assumptions, the detection of post-harvest growth relies on geometric and radiometric features derived from XYZ coordinates and signal amplitude considering the local neighborhood of each laser point. To specify the amplitude threshold A_T for the calculation of the amplitude density feature, a first exploratory analysis was performed by calculating statistics and distribution functions of the extracted training data. The local neighborhood was defined as spherical neighborhood, thus Euclidean metric in 3D with a fixed distance threshold (Filin & Pfeifer, 2005). Because of the different shapes of post-harvest growth objects, nine local neighborhood features were calculated with four distance thresholds (R) (0.002 m, 0.005 m, 0.02 m, 0.05 m) and with the derived amplitude threshold. The feature calculation results in 36 additional features attached to each laser point. The final feature space comprises 38 features in total (Tab. 1): nine features calculated with four different distance thresholds, plus the corrected amplitude and Riegl's deviation. The importance of the computed features and their impact on the classification were assessed in the feature correlation analysis as well as in the model construction and model application.

Table 1. List of single laser point features derived in local neighborhood for classification considering the search radius R and amplitude A_T.

Symbol	[Unit]	Description
A	[DN]	Corrected signal amplitude
EW		Riegl's deviation (pulse shape of the echo signal compared to the pulse shape representing the so-called system response - area below the shape curve)
Concerning local neighborhood:		
ER	[%]	Echo ratio (ratio of number of points in 3D and in 2D)
A_{dens}	[%]	Amplitude density (percentage of points with amplitude lower than threshold)

A_{cov}	[DN]	Coefficient of variation of all amplitude values
A_{mean}	[DN]	Mean amplitude of all amplitude values
Dz	[m]	Elevation difference between the single point and the minimum elevation value
StdZ	[m]	Standard deviation of all elevation values
Zdiff	[m]	Range of maximum and minimum elevation value
Nbs2D		Number of neighboring points in 2D (planimetric)
Nbs3D		Number of neighboring points in 3D (sphere)

3.1.3. Data Correlation Analysis

To assess whether the calculated features are measuring the same construct, i.e. whether they are redundant, a correlation analysis was performed. The analysis evaluates the pairwise correlation between all features of the feature space (Tab. 1). With respect to the degree of correlation, three cases can be assumed: 1) high correlation as an indicator of redundant features (e.g. already linked in calculation), 2) high correlation of features whose combination describes an object characteristic and 3) low correlation as an indicator of independent features. The correlation and possible redundancies between single features were analyzed by using the Pearson's product-moment correlation coefficient (PCC) and the principal component analysis (PCA).

The PCC computes the correlation between all features and produces a weight vector based on these correlations (Pearson, 1895). The degree of association between two features is given as a number between -1 (negatively correlated) and +1 (positively correlated). No correlation is indicated with a value equal to 0. The PCA performs a dimensionality reduction using the covariance matrix (Jolliffe, 2002). The procedure searches for k n-dimensional orthogonal vectors that can be used to represent the data ($k \leq n$) most adequately. It converts possibly correlated attributes into a set of values of uncorrelated features (principal components), which are ordered by decreasing significance.

3.2. Classification

The classification aimed at extracting a model that predicts the class label 'post-harvest growth' from TLS data. Different machine learning techniques for the classification were tested: 1) supervised classifiers (tree induction and Naïve Bayes), and 2) unsupervised classifier (k-Means) considering the geometric features, the radiometric features, and a combination of geometric and radiometric features. The usage of different approaches on the one hand prevented the usage of classification rules derived from over-fitted modeling of one classifier, and on the other hand substantiated the possibility of classifying the point cloud on the basis of different classification principles. The approaches were selected based on the similar application of those for surface classification (Alexander et al., 2010; Gerke & Jing, 2014; Pal & Mather, 2003), vegetation detection in airborne (Ducic et al., 2006; Höfle & Hollaus, 2010; Rutzinger et al., 2008; Zlinszky et al., 2012) and in terrestrial LiDAR data (Koenig et al., 2013).

Cluster analysis like *k*-Means has been used in ALS applications such as tree detection (Lindberg et al., 2013; Vauhkonen et al., 2012).

Data classification for each technique was performed in two-steps: 1) the learning step, where the classification model was constructed based on training data, and 2) the classification step, where the model assigned the class labels.

3.2.1. Model Construction

To predict the best class label within the supervised classification, the training data were portioned relatively with a ratio of 0.7 by stratified sampling, based on Gini Index Weighting (Breiman, 2001). 70 percent of the data were used in the training sub-process (model learning) and 30 percent in the testing sub-process (model testing).

The advantage of tree induction lies in the straightforward handling to construct classifiers with no requirements in domain knowledge or parameter setting. Additionally, it requires no assumptions regarding distribution of input data and provides an intuitive way to interpret classification structure (Hansen et al., 1996). The decision tree was generated by recursive partitioning, using a minimal size for split of four and a minimal leaf size of two. As criterion for tree induction the gain ratio was chosen with minimal gain of 0.1 and confidence of 0.25. To prevent an over-specific or over-fitted tree, pre-pruning with three alternative nodes for splitting was chosen. The gain ratio is a variant of information gain and adjusts the information gain for each attribute allowing the breadth and uniformity of the attribute values (Quinlan, 1986). Additionally, in the case of random forest (RF) analysis, the number of trees was set to 20. The precision of the applied RF depends on the strength of the individual classifiers and the measure of the dependence between them. Every tree of the RF consists of a different set of learning data, which can result in differences in accuracy towards the overall accuracy. The predominant usage of features for discrimination within the RF denotes the features' significance.

The Naïve Bayes classifier is based on a probability model and requires only a small amount of training data. The advantage lies in the assumption of independent features, whereby only the variance of the features for each class label needs to be determined and not the entire covariance matrix (Zhang, 2004). Laplacian correction was used to avoid probability values of zero.

Unlike in classification, the class label is unknown in cluster analysis. Clustering groups a set of data objects into multiple clusters such that objects within a given cluster have high similarity, but are very dissimilar to objects in other clusters. The similarity is based on a measure of distance in feature space. The most fundamental and simplest cluster analysis is partitioning, which organizes the objects into several exclusive clusters. It is an effective clustering method for small-size data sets (Han et al., 2012). In this study we used *k*-Means, a centroid-based partitioning technique, to find the mutually exclusive clusters. With a pre-defined number of clusters ($k = 2$) and Bregman Divergence with Squared Euclidean Distance (Banerjee, 2005) as distance measure, the cluster analysis run with maximal 1000 iterations for one of the 100 runs of *k*-Means. To assess the feasibility of the applied *k*-Means, the silhouette coefficient (SC) was applied. The SC measures the compactness of a cluster and the separation towards other clusters

(Rousseeuw, 1987). For each object in the dataset, the average distance between the object and all other objects in the cluster was calculated.

3.2.2. Accuracy Assessment and Model Application

The accuracy of the resulting models was assessed by calculating precision (p), recall (r), Cohen's kappa (κ), and error rate (e) (Equation (1)-(4)). Precision, recall, and κ are better suited to the class imbalance problem, where the main class of interest (post-harvest growth) is rare. Precision (user's accuracy) represents the exactness, i.e. the percentage of tuples correctly labeled as 'post-harvest growth', whereas recall (producer's accuracy) is a measure of completeness, i.e. the percentage of post-harvest growth tuples, which are labeled as such. The κ (Cohen, 1960) was used as a measure of the quality of the binary classification, representing the agreement between the two raters 'ground' and 'post-harvest growth' within LiDAR-based classification on the one hand and between the two raters 'LiDAR-based classifier' and 'RGB image-based classifier' for the class of 'post-harvest growth' on the other hand. The model with the best performance was used within the subsequent classification procedure.

$$\text{Precision}^{*1} = TP / (TP + FP) \quad (1)$$

$$\text{recall}^{*1} = TP / (TP + FN) \quad (2)$$

$$\kappa^{*1} = (P(a) - P(e)) / (1 - P(e)) \quad (3)$$

$$\text{error rate}^{*1} = (FP + FN) / (TP + FP + FN + TN) \quad (4)$$

$$\text{accuracy}^{*2} = (TP + TN) / (TP + FP + FN + TN) \quad (5)$$

In Equations (1-5), TP is the number of true positives, TN the number of true negatives, FP the number of false positives, FN the number of false negatives, *P(a)* is the relative observed percentage of agreement among the raters and *P(e)* is the expected percentage of agreement.

3.3. Evaluation

The evaluation of post-harvest growth detection was performed at various levels, involving the classifier itself as well as the comparison with the reference data of classified RGB image and calculated NDVI of hyperspectral data.

3.3.1. Evaluation of the derived classification rules by reference data

The classified point cloud was evaluated by comparison with the classified image of: 1) cell-by-cell error assessment; and 2) calculated total post-harvest growth area coverage in percent of sample plot one. For the cell-by-cell error assessment, binary raster maps of the classified point cloud were derived, taking the most frequent class of the laser points within a raster cell. The cell size was set to 0.005 m based on the average

[1] used for evaluation within model construction
[2] used for evaluation with reference data

point distance of the point cloud. However, varying point distribution and shadowing effects in certain areas of the TLS data confined the comparison of rasterized coverage to cells that have values in the LiDAR-derived case. The accuracy (Equation 5) as a measure of the closeness of TLS to the RGB classification (true) was calculated. Furthermore, area coverage per Penta-Spek footprint was calculated from the binary raster maps to relate the amount of vegetation coverage with $NDVI_{705}$.

3.3.2. Evaluation of the transferability of derived classification rules and of the effect of point density on classification

The transferability of derived classification rules from training data to remaining field data was performed by rule allocation to a second sample plot (test data) 20 m distant from the training data location. In order to assess the precision of the classification via TLS, the effect of point density on classification performance, due to different scanning distance, was assessed using five single scan positions located around the training data. For each point dataset variant, the same processing steps of feature calculation, correlation analysis, and model construction were performed. Due to decreasing point density and increasing mean point distance, the local features of single laser points of Tab. 1 were calculated within a search radius R of 0.02 m, 0.05 m and 0.1 m and with derived amplitude thresholds A_T per scan position (Tab. 6).

4. Results and Discussion

4.1. Radiometric Correction of Signal Amplitudes

The data-driven range correction of signal amplitudes shows the lowest RMSE (2.1%) for a polynomial of degree seven (Fig. 3). The maximum recorded amplitude is reached at a distance of approximately 10 m, and decreases with distance thereafter. This indicates a polynomial approximation, as well as certain homogeneity of the used natural surfaces. Comparing the coefficient of variation of all amplitude values for all scan positions before and after correction, a reduction from 7.1% to 2.7% is given. The remaining variation can be explained by a certain roughness of the natural terrain (Höfle, 2014).

The evaluation of the range correction was based on one reference target with known and constant reflectance placed in each scan position. After the range correction, the calculated standard deviation of all target medians shows lower value (1.10%) compared to the standard deviation before the range correction (4.13%). Additionally, the performance was visually explored by comparing the point cloud colored by uncorrected and corrected amplitude values (Fig. 4). The comparison shows the successful elimination of the range effect. Due to higher variation, scan position three was excluded for further analysis.

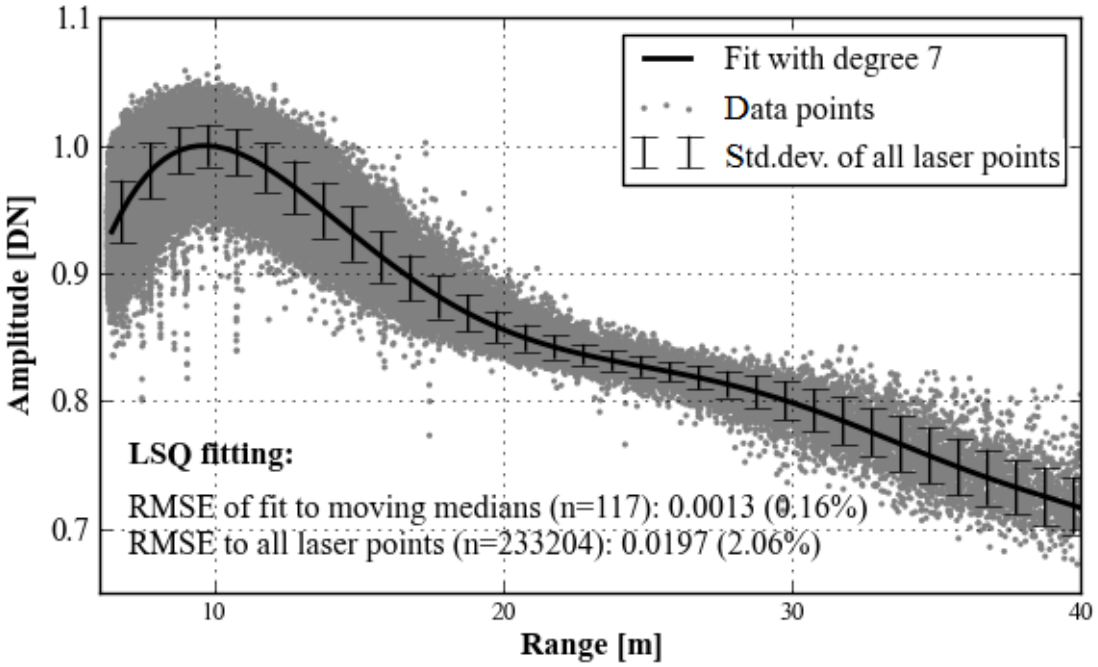

Fig. 3. Polynomial function of range-amplitude dependency assessed by Least-Squares (LSQ) fitting to moving median values of original amplitudes derived by field data.

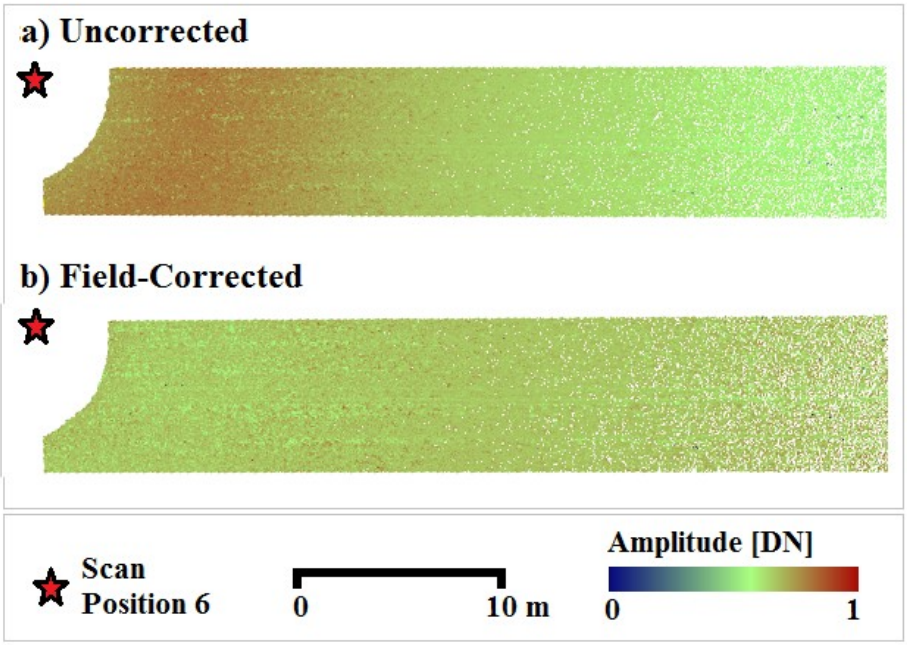

Fig. 4. Comparison of amplitudes (a) before and (b) after radiometric correction based on field-derived correction function, showing scan position six.

4.2. Feature Extraction and Correlation Analysis

Already the corrected signal amplitude A shows a high separability between ground and post-harvest growth with amplitude ≤0.783 DN for post-harvest growth, which can clearly be seen by the colored distribution functions (DF) in Fig. 5. This separability is confirmed by an applied decision tree (DT) considering only the amplitude values. The DT defines post-harvest growth with amplitude ≤ 0.767 DN with a precision of 94.3%. Both approaches exhibit lower signal amplitude values for post-harvest growth

with a slightly differing threshold. The difference between DF and DT can be explained on the one hand by the applied moving median in DF, resulting in a different threshold depending on the overlap parameter used, and on the other hand by the DT taking the overlapping area for distinction into account. The threshold A_T derived by DT (0.767 DN) was used to calculate the features listed in Tab. 1. In general, the lower signal amplitude may be explained by the low reflectance of plants at 1550 nm. The plants' reflectance spectrum is, among other things, influenced by the water content which shows higher absorption around 1500 nm and results in lower reflectance compared to dry ground (Fabre et al., 2011). Dry soil as well as crop residues' dry matter, on the other hand, are spectrally similar (Streck et al., 2002), and show increasing amplitude with decreasing moisture (Daughtry & Hunt, 2008; Whiting et al., 2004).

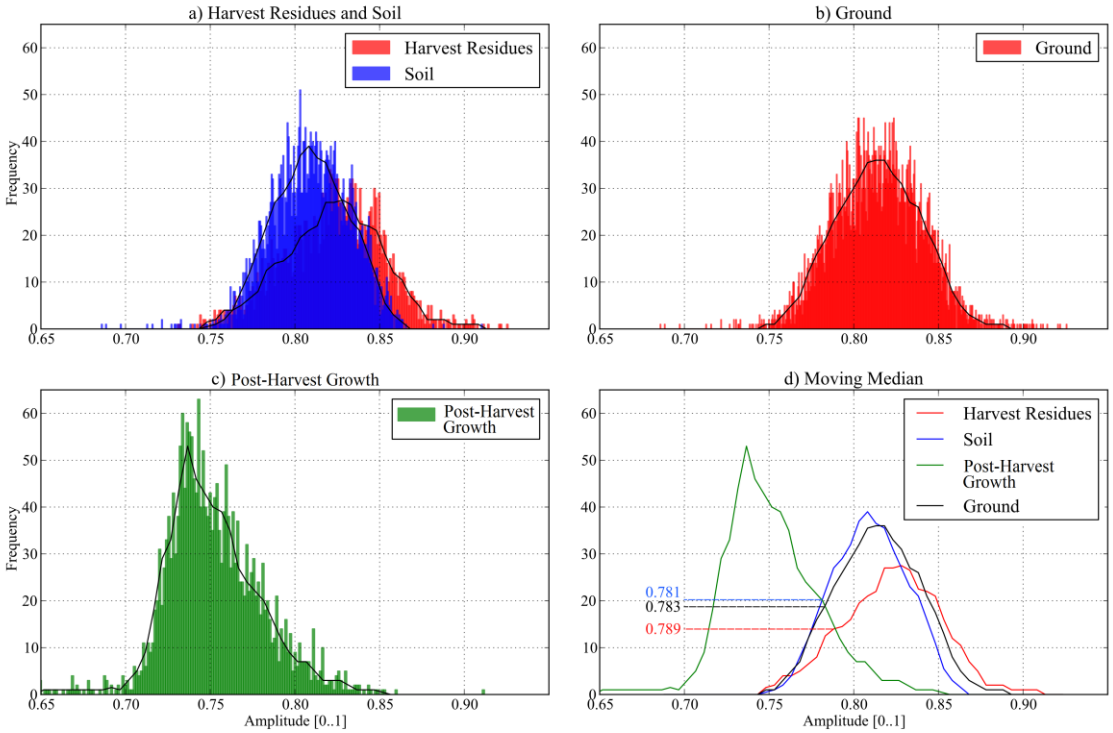

Fig. 5. Distribution function of corrected amplitude of the different classes occurring in field data: (a) Harvest residues and soil; (b) ground (harvest residues and soil); (c) post-harvest growth and (d) moving median of all classes and the resulting threshold.

Correlation analysis was applied to identify the similarity of the features in the feature space. The features ER, A_{cov}, and number of points in 2D and 3D show low to high correlation. High correlation is represented in both sides of correlation degrees: 1) the expected positive correlation (PCC = 0.9) between StdZ and Zdiff; and 2) negative correlation (PCC < -0.7) between the amplitude-based features (A, Amean) and Zdiff. The second group of correlations reflect the characteristics of ground and post-harvest growth. For example, post-harvest growth is characterized by lower amplitude values considering Fig. 5 and by distinct elevation differences compared to ground.

The Gini Index Weighting as well as the features included in the calculated principal components can be used to predict the explanatory power of the features; the Gini Index as a measure of inequality and PCA as measure of the variance of features. The most relevant features according to Gini Index Weighting are A_{mean}, A_{dens}, A,

followed by *Zdiff* and *StdZ* (cf. Fig. 6), with higher weights for radiometric features than geometric features. According to the PCA, the most relevant features are the number of neighboring points within a 5 cm search radius and A_{dens}. The features weighting by PCA shows a significance of 0.7 for *Nbs2D* and *Nbs3D* and for A_{dens} significances of 0.4 to 0.5. All the other features follow with a significance of less than 0.2.

The correlation analysis underlines the potential of radiometric features as well as the consideration of the local neighborhood of points for distinction of ground and post-harvest growth. Post-harvest growth tends to lower amplitude values and elevation differences up to 12 cm compared to ground. The results are comparable to former studies where A_{mean} and the *StdZ* are chosen for vegetation classification (Höfle, 2014; Koenig et al., 2013; Rutzinger et al., 2008).

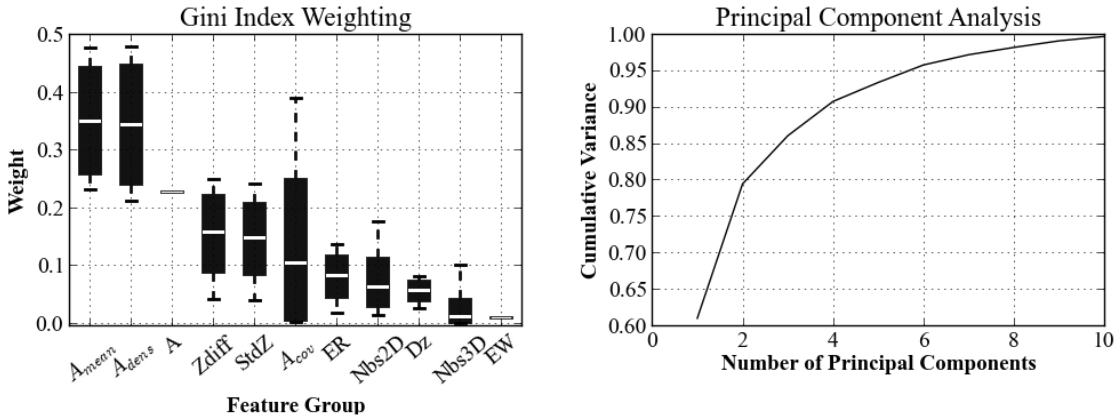

Fig. 6. Feature importance by Gini Index Weighting (left) per feature group and by PCA (right).

4.3. Classification

In order to achieve the best accuracy and to test the power of the derived feature groups, three subsets of feature groups from the training data were chosen: 1) geometric features; 2) radiometric features; and 3) a combination of geometric and radiometric features.

The most reliable classification is achieved by using the combination of geometric and radiometric features, resulting in >99% precision (Tab. 2). Adding geometric features leads to a small increase in precision for the unsupervised classifiers and it reduces the error rate by 0.7%. Both tree induction classifiers predominantly discriminate the post-harvest growth by A_{dens} as the first node, and the node with the largest size, and in subsequent order by the geometric features such as standard deviation in elevation *StdZ* (Fig 7). The most frequently used features are in the search radius of 0.02 m and 0.05 m. The derived amplitude thresholds of 0.772 ± 0.007 DN are comparable within the tree induction.

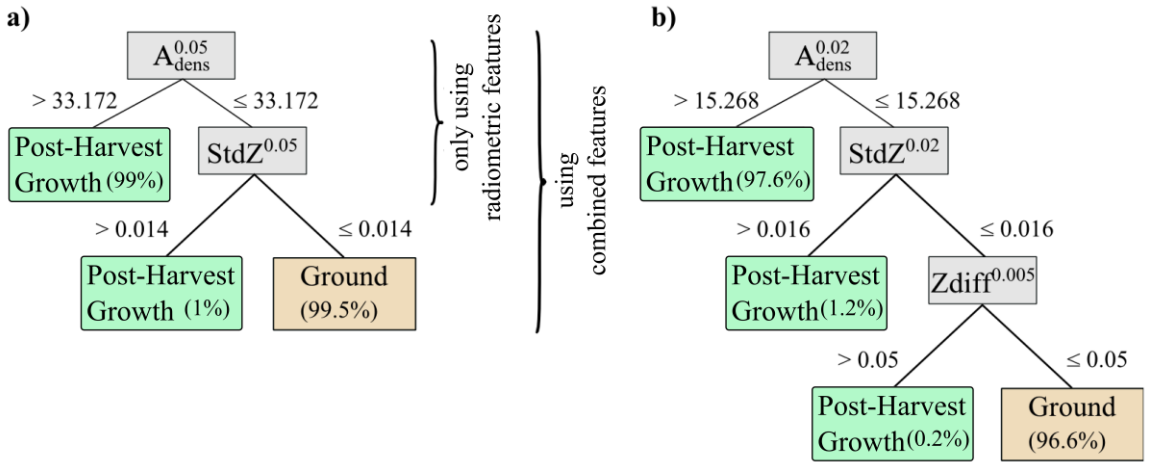

Fig. 7. Derived classification tree of training data, which achieved the highest precision from decision tree (a) and random forest (a)(b). The amount of true positives per class at each leaf node is given in brackets.

Table 2. Results of supervised classification (precision (p), recall (r), Cohen's kappa (κ), error rate (e)). For random forest, the overall accuracy for 20 trees is given as well as the coefficient of variation of all trees in brackets.

Features		Supervised classifier		
		Decision Tree	Random Forest	Naïve Bayes
Corrected value of signal amplitude	p	94.3%	93.8% (1.2%)	88.3%
	r	72.7%	72.7% (3.0%)	80.7%
	κ	0.65	0.65 (0.05)	0.66
	e	17.8%	18.0% (19.1%)	16.8%
Geometric features	p	88.1%	96.4% (11.9%)	81.5%
	r	95.9%	76.8% (27.9%)	79.3%
	κ	0.80	0.71 (0.21)	0.69
	e	9.5%	14.6% (40.7%)	15.8%
Radiometric features	p	99.5%	99.0% (2.5%)	98.2%
	r	99.4%	99.0% (7.8%)	99.2%
	κ	0.98	0.98 (0.10)	0.97
	e	0.7%	1.1% (127.2%)	1.5%
Geometric + radiometric features	p	99.9%	99.0% (6.3%)	98.7%
	r	100.0%	99.6% (11.0%)	99.7%
	κ	0.98	0.98 (0.19)	0.98
	e	0.0%	0.8% (123.4%)	0.9%

Applying the *k*-Means, the combination of geometric and radiometric features shows a weak silhouette coefficient and low precision compared to using solely radiometric features for the whole training dataset ($SC_{combined}$ 0.4 < $SC_{radiometric}$ 0.7 and $p_{combined}$ 52.4% < $p_{radiometric}$ 61.4%) (Tab. 3). The weaker SC of using the combination of geometric and radiometric features is due to small elevation differences of post-harvest growth and ground points.

Table 3. Error assessment of cluster analysis (*k*-Means) of labeled training data using subset 2 (radiometric features) and subset 3 (combined geometric and radiometric features).

		Class		Silhouette coefficient	
		Post-Harvest Growth	Ground	Range [min;max]	Mean ± Std
Subset 2	Cluster 1 (Ground)	57.1%	41.3%	[0.01;0.85]	0.76 ± 0.14
	Cluster 2 (Post-Harvest Growth)	61.4%	38.6%	[0.01;0.81]	0.69 ± 0.19
	Precision	61.4%			
	Recall	57.1%			
	Kappa	0.03			
	Error rate	47.5%			
Subset 3	Cluster 1 (Ground)	47.6%	62.2%	[-0.02;0.61]	0.43 ± 0.15
	Cluster 2 (Post-Harvest Growth)	52.4%	37.8%	[-0.06;0.55]	0.36 ± 0.16
	Precision	52.4%			
	Recall	63.8%			
	Kappa	0.15			
	Error rate	43.3 %			

The benefit of combining geometric and radiometric features of a local neighborhood to distinguish between ground and post-harvest growth is deduced from comparing the results and the tendency of increasing precision of the applied classifiers. The relevance of the local radiometric features is also reflected in the Gini Index Weighting and the PCA (Fig. 6). Small elevation differences of ground and post-harvest growth lead to a lower impact of geometric features for classification. In the case of higher plants, the power of geometric features increases, which was also shown in others studies of vegetation detection (Andújar et al., 2013; Höfle, 2014; Lumme et al., 2008).

4.4. Evaluation with Reference Data

The evaluation proceeded on two levels to demonstrate the potential of using LiDAR data for classification: 1) cell-wise comparison and comparison of calculated area coverage of LiDAR and of RGB image classification and 2) calculated coverage of LiDAR and RGB in relation to the calculated $NDVI_{705}$ within the footprint of hyperspectral sensor of sample plot one. Due to varying spatial resolution and data models of different datasets, coverage raster maps were computed and compared.

4.4.3. Comparison with RGB Image Classification

The calculated coverage of post-harvest growth of the sample plot varies from 3.6% to 19.2% for TLS based classification, while the RGB image analysis shows coverage of 5.1% (Tab. 4). The best match in coverage is reached by Naïve Bayes and tree induction (Fig. 8b-d), whereas the *k*-Means overestimates the post-harvest growth

coverage using the combination of geometric and radiometric features. The small overestimation in Naïve Bayes and tree induction results from considering the local neighborhood and its effect within the transition area of post-harvest growth and ground. In comparison to the *k*-Means, Naïve Bayes and tree induction have detected the majority of the post-harvest growth patches with higher precision (Tab. 5). Applying only radiometric features, *k*-Means achieves comparable results (Fig. 8e) and a coverage value of 3.6%. A cell-by-cell error assessment of LiDAR-derived classes and classes derived by image analysis yields a high precision of >77% (Tab. 5), considering only cells with a label in LiDAR maps. The cell-by-cell error assessment of LiDAR and the RGB image can only be used to some extent due to misclassification in the RGB classification process or due to effects caused by downscaling the resolution of the RGB image. The calculated coverage per defined area in contrast provides a good indication of the amount of post-harvest growth.

The transferability of the derived classification rules to the whole field can be seen in the test data of another sample plot 20 m distant from the training data. A comparison of the classified point cloud and the corresponding RGB image (Fig. 9) shows agreement with the allocation of small post-harvest growth patches.

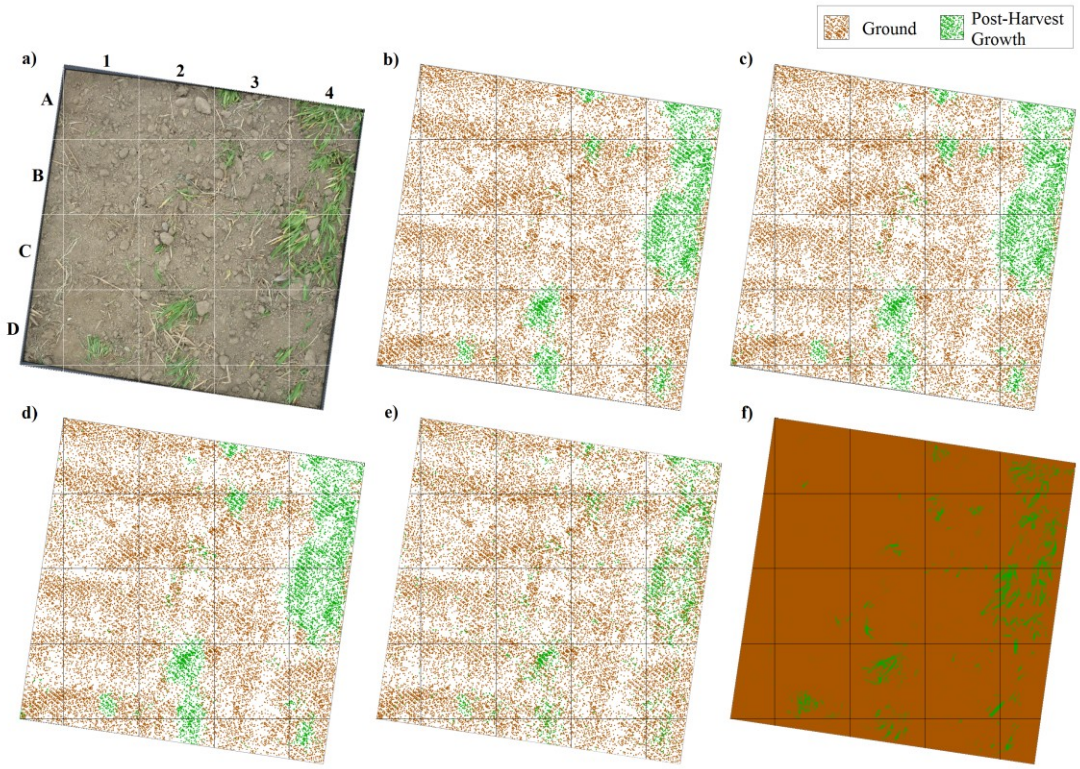

Fig. 8. Classified sample plot 1 (1m²): (a) RGB image; (b) classified by DT; (c) classified by RF; (d) classified by Naïve Bayes analysis using geometric and radiometric features; (e) classified by *k*-Means using radiometric features and (f) classified by RGB.

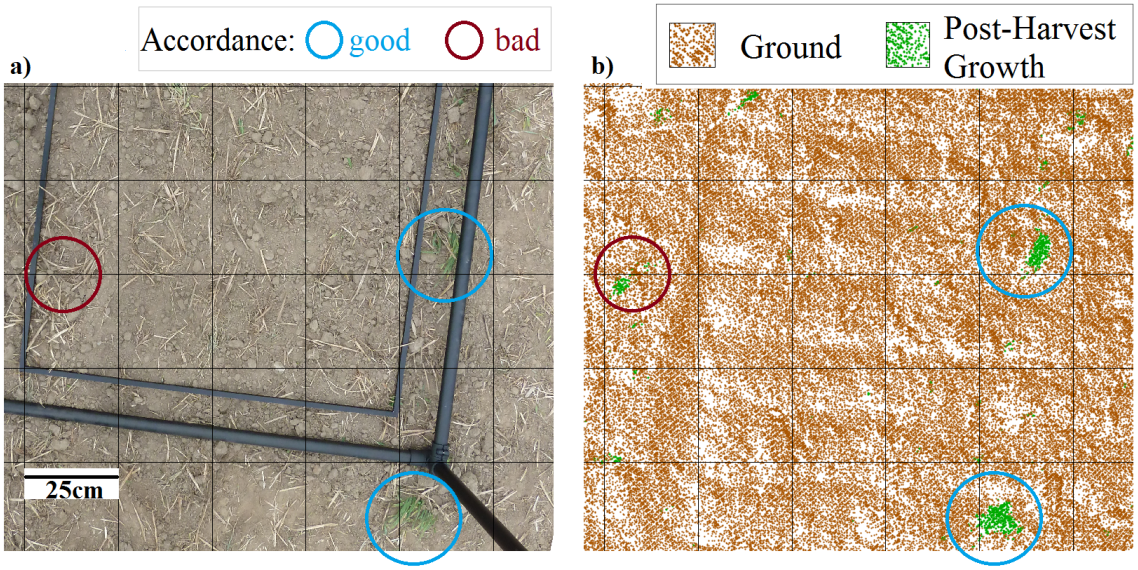

Fig. 9. Classified sample plot 2 (1m²), marked with good and bad accordance: (a) RGB image; (b) classified by RF.

Table 4. Resulting ratio of post-harvest growth points and resulting coverage at cell size of 0.005 m. The calculation based on the classification by using a combination of geometric and radiometric features and for *k*-Means by using radiometric features, additionally given in brackets. Coverage is given as the percentage of post-harvest growth points within sample plot one. The remaining percentage represents areas with no point classification.

Data set	**Coverage**	
	Post-harvest growth	**Ground**
3D point cloud (ratio of number of points per class)		
1) Decision Tree	21.5%	78.5%
2) Random Forest	22.4%	77.6%
3) Naïve Bayes	21.5%	78.5%
4) *k*-Means	47.4% (13.3%)	52.6% (86.7%)
2D binary raster maps		
1) Decision Tree	6.8%	29.5%
2) Random Forest	7.1%	29.3%
3) Naïve Bayes	6.6%	29.7%
4) *k*-Means	19.2% (3.6%)	17.2% (32.7%)
RGB-image analysis	5.1%	94.9%

Table 5. Error assessment of cell-by-cell comparison between the rasterized maps of LiDAR and RGB classification (positive predictive class 'post-harvest growth').

		Supervised classifier			Unsupervised classifier
		Decision Tree	Random Forest	Naïve Bayes	k-Means (radiometric feat.)
accuracy	a	77.3%	81.2%	80.9%	89.9%
precision	p	83.3%	91.7%	91.7%	50.0%
recall	r	0.18%	0.24%	0.25%	0.24%
kappa	κ	0.32	0.41	0.41	0.30
error rate	e	22.7%	18.8%	19.1%	10.1%

4.4.3. Comparison with NDVI

All applied classification methods detect and locate post-harvest growth precisely. The NDVI as an indicator for the vitality of vegetation may be reflected in the coverage of green vegetation. The regression analysis of $NDVI_{705}$ with calculated coverage per classification method shows a polynomial correlation of degree 2 within sample plot one (Fig. 10). The higher coverage, in the upper right area of the sample plot (Fig. 8, A4 and C4), is reflected in a higher $NDVI_{705}$ of >0.17. The highest coefficient of determination (R^2) of 0.80 is achieved by image analysis followed by all LiDAR-based classifiers with R^2 of 0.71 ± 0.03.

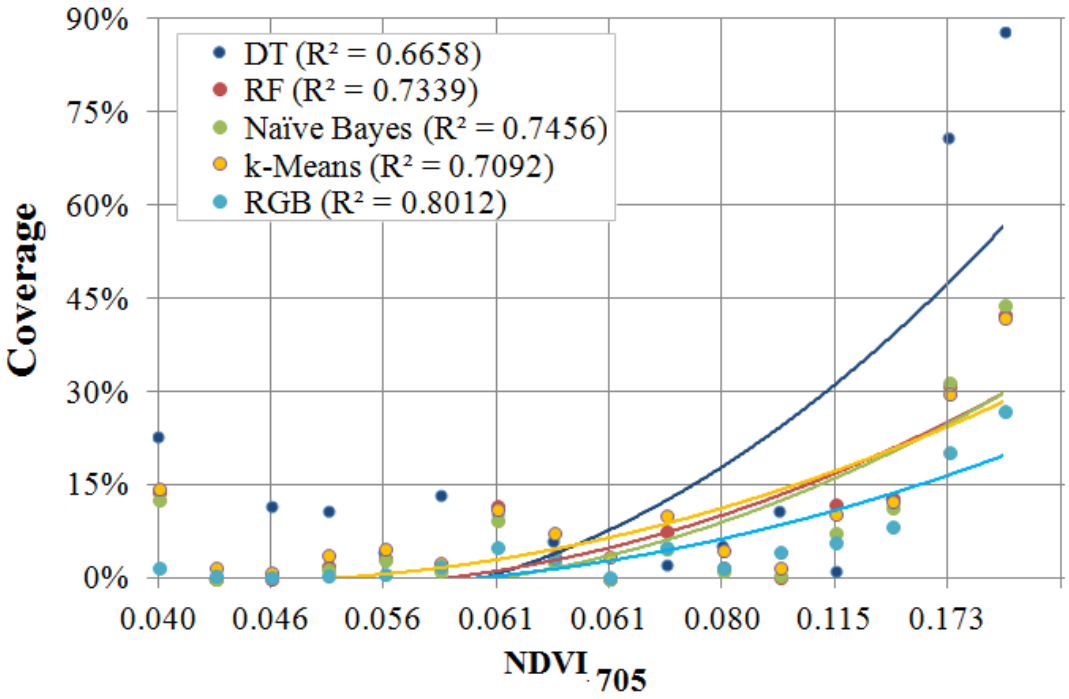

Fig. 10. Polynomial regression (degree 2) and R^2 between $NDVI_{705}$ and post-harvest growth coverage (%) estimated by LiDAR data and RGB-image analysis within the sample plot one.

4.5. Effect of Point Density on Classification

To evaluate the heterogeneous point density of static TLS and its effect on the applied post-harvest growth classifications, tests concerning the scan distances and

resultant differences in point density were performed. Compared to ground within all scan positions, the training data shows similar behavior of lower mean amplitude values for post-harvest growth (Tab. 6). The thresholds derived from the decision tree and from the density function differ slightly (±1%) from the threshold derived from the whole data (dense data). According to the calculated weights of the Gini Index, the higher importance of radiometric features compared to geometric features within all distances are also given (Fig. 11). However, the importance of radiometric features decreases with increasing distance from >0.4 (~ 12 m) to <0.35 (~25 m). A possible explanation is the increasing mean point distance and the subsequently lower similarity of amplitudes between all points within the search radius compared to elevation differences. Especially the transition from ground to post-harvest growth with lower intermediate steps in elevation shows higher values of standard deviation of elevation and lower mean amplitude. The gain in importance of geometric features can be seen for scan position six in higher weights of *Dz* and *StdZ*. Within each scan position, A_{dens} and *Dz* are the most relevant features, which corresponds to the results of using dense data.

Scan position four shows different behavior in the importance of the features of the two target classes. In consequence of the mean distance of 30 m of the scan position four and corresponding to the distance limitation of 30 m, the training data are reduced and post-harvest growth patches with larger elevation values are not considered. This reduction results in the lower importance of geometric features for classification.

The assigned rules derived by DT to the point cloud of sample plot one for scan positions 1, 2, 4, and 5 show a good agreement to the DT classification of dense data (Fig. 12) and to the calculated post-harvest growth coverage of 12.3% ± 0.6% (Tab. 8) at 0.02 m resolution. The larger post-harvest growth patches of larger than 10 x 10 cm are classified by all scan positions, whereas smaller patches (e.g. Fig. 12, B2) are often not detected by the derived rules. The derived model of scan position six results in higher misclassification of ground points (Fig. 12e, C3).

The benefit of using the combination of geometric and radiometric features and the necessity of distance limitation is underlined when investigating the classification results based on the data with different point densities. Larger post-harvest growth patches can be classified by having at least a point density of 2 pts./0.01 m². It can be summarized that higher point densities allow for the detection of smaller post-harvest growth patches.

Table 6. Characteristics of training data per scan position.

	Position 1	**Position 2**	**Position 4**	**Position 5**	**Position 6**
Mean distance [m]	12	21	30	15	25
Mean incidence angle to surface normal [°]	70	79	82	74	81
Mean point density [pts/0.01m²]	9	2	2	13	1
Amplitude threshold [DN] (DT)	0.776	0.790	0.766	0.764	0.810
Amplitude threshold [DN]	0.779	0.783	0.777	0.770	0.794

(DF)					
Mean Amplitude [DN]					
Ground	0.802	0.810	0.791	0.824	0.807
Post-Harvest Growth	0.755	0.776	0.703	0.750	0.794

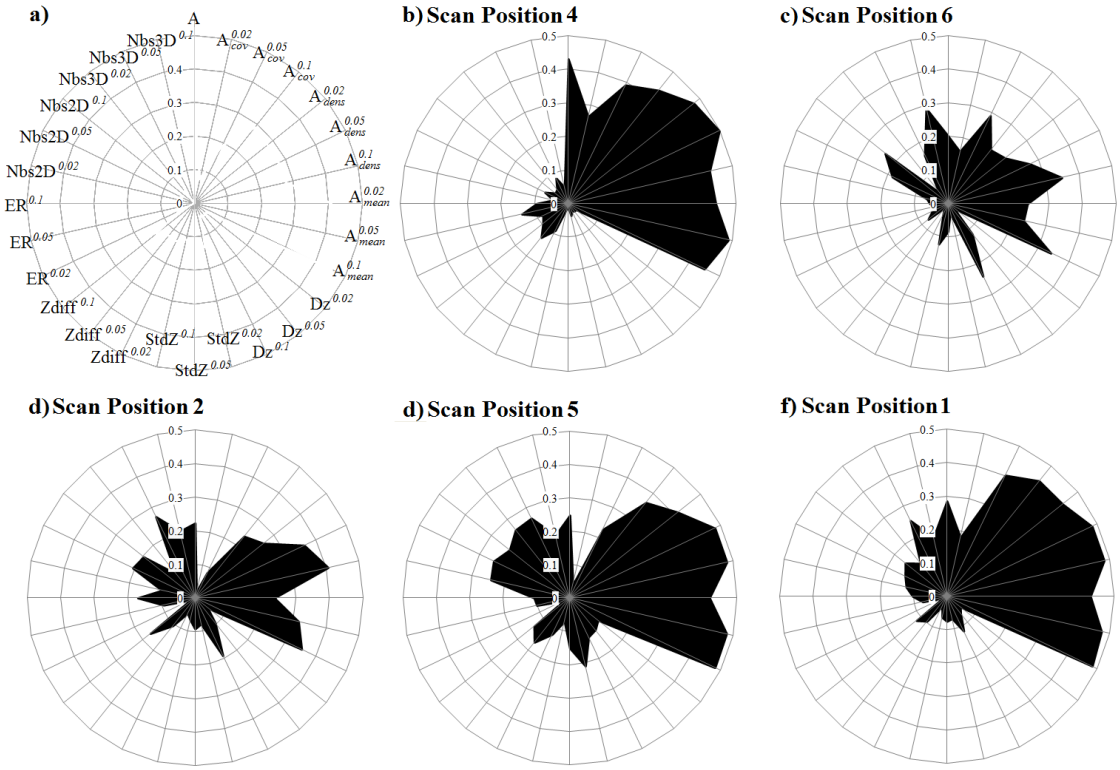

Fig. 11. Feature importance of spatial features by Gini Index per scan position, without position 3; (a) features; (b)-(f) ordered by decreasing distance.

Table 7. Distance dependent DT classification (precision (p), recall (r), Cohen's kappa (κ), error rate (e)) of single scan positions.

		Position 1	Position 2	Position 4	Position 5	Position 6
Corrected value of signal amplitude	p	95.7%	95.0%	100.0%	94.4%	97.6%
	r	48.0%	81.6%	92.4%	77.0%	59.7%
	κ	0.72	0.71	0.90	0.69	0.56
	e	47.0%	15.2%	3.6%	15.9%	20.4%
Geometric features	p	83.2%	93.9%	68.2%	97.9%	100.0%
	r	91.1%	94.5%	97.8%	87.6%	77.6%
	κ	0.74	0.79	0.56	0.78	0.80
	e	14.5%	7.8%	22.8%	8.2%	11.0%
Radiometric features	p	98.9%	95.9%	100.0%	100.0%	90.4%
	r	100.0%	100.0%	100.0%	100.0%	98.5%
	κ	0.98	0.97	1.0	0.99	0.71
	e	0.7%	2.9%	0.0%	0.0%	5.8%
Geometric +	p	98.9%	95.9%	100.0%	99.6%	89.3%

radiometric features	r	100.0%	100.0%	100.0%	100.0%	100.0%
	κ	0.98	0.97	1.0	0.99	0.66
	e	0.7%	2.9%	0.0%	0.2%	5.8%

Table 8. Resulting coverage of post-harvest growth for different scan positions at cell size of 0.02 m. The calculation based on DT classification by using a combination of geometric and radiometric features. Coverage is given as the percentage of post-harvest growth points within sample plot one.

	Position 1	**Position 2**	**Position 4**	**Position 5**	**Position 6**	**All**
Post-Harvest Growth	12.0%	12.9%	5.7%	11.9%	12.7%	12.9%
No Data	28.3%	22.4%	63.6%	29.7%	74.9%	22.4%

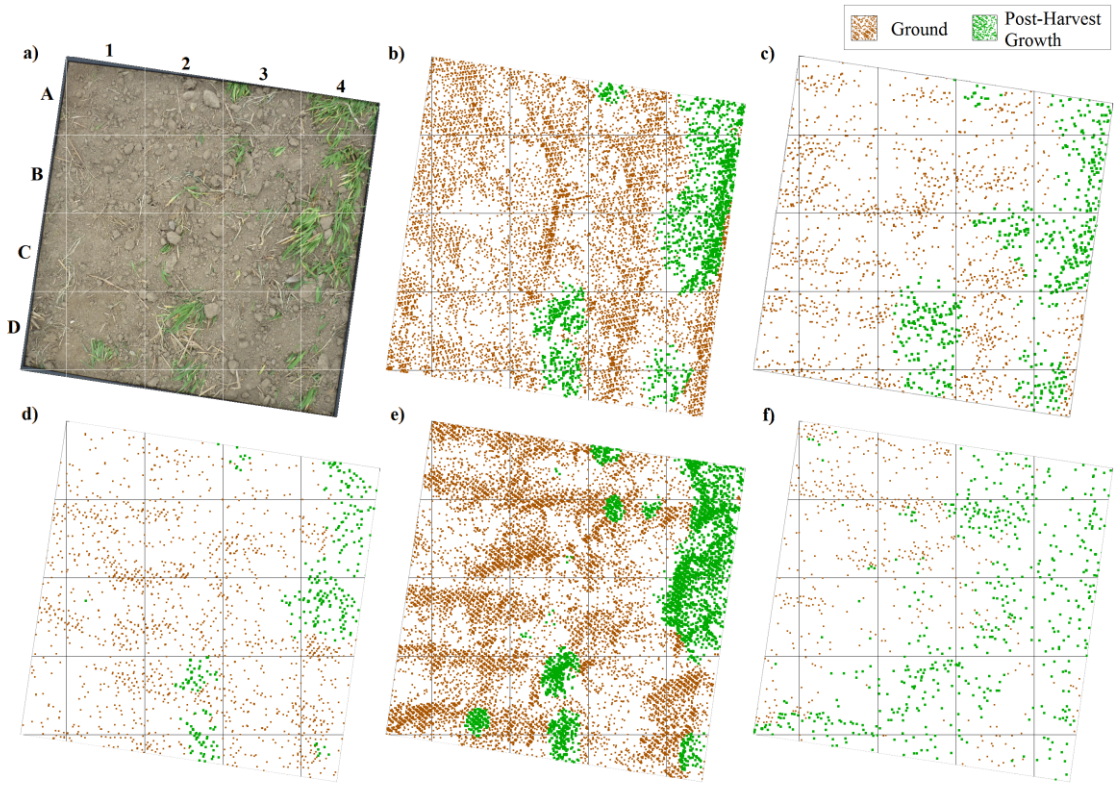

Fig. 12. Classified sample plot 1 (1m²): (a) RGB image; (b)-(f) scan position 1-6 (without position 3) classified by DT analysis using geometric and radiometric features.

5. Conclusion

The findings of this paper confirm the potential of using TLS and the combination of derived geometric and radiometric information for the detection of post-harvest-growth patches. This supports the outcomes of Andújar *et al.* (2013) and Höfle (2014). By using radiometric information in combination with geometric information it is even possible to detect objects of low elevation difference. The radiometric correction of the distance effect was possible by using natural reference targets (bare soil transect), reducing the standard deviation of amplitude of homogeneous areas (e.g. reference targets

of Spectralon®) from 4.3% to 1.1% on average. The separability between the two target classes 'post-harvest growth' and 'ground' is confirmed by comparative classification analysis. High precision of > 99% is reached in model construction for all supervised classifiers. Furthermore, comparable post-harvest growth coverage values are derived by LiDAR (~ 7%) compared to coverage of 5% by RGB image classification. The benefit of using radiometric information in object detection is shown by the improved precision in classification of up to 99% and the reduced error rate of <0.1% compared to a precision of <88% and error rate of >9% without using radiometric information. Even a low point density of 2 pts. / 0.01 m² is sufficient for the detection of larger post-harvest growth patches (10 x 10 cm), confirmed by a precision of >96% and an error rate of <2.9% within DT classification.

Acknowledgments

This work was partly funded by the Federal Ministry of Science, Research and Arts (MWK), Baden Württemberg, in the framework of the project LS-VISA (FKZ 1222 TG 87), by the Federal Ministry of Economics and Technology (BMWi), Germany, in the framework of the project "HyLand" (FKZ 50EE1014), and by the Federal Ministry of Food, Agriculture and Consumer Protection (BMELV), in the framework of the project 'ESOB'. The authors would like to thank C. Klonner, J. Profe, J. Lauer (GIScience Research Group, Institute of Geography, Heidelberg University) as well as N. Richter (Julius-Kühn-Institute for Crop and Soil Science, Braunschweig) for helping in the field campaign and compilation of this paper.

Author Contribution

Kristina Koenig and Martin Hämmerle, Thomas Jarmer and Holger Lilienthal were responsible for the field data collection. The image classification was performed by Thomas Jarmer and Bastian Siegmann. The hyperspectral data collection and processing was performed by Holger Lilienthal. Kristina Koenig, with input from Martin Hämmerle and Bernhard Höfle, designed and conducted substantial parts of the analysis and wrote the article. Bernhard Höfle contributed the overall research design of the study. The article was improved by the contributions of all the co-authors at various stages of analysis and writing process.

Conflicts of Interest

The authors declare no conflict of interest.

References

Alexander, C., Tansey, K., Kaduk, J., Holland, D., Tate, N.J., 2010. Backscatter coefficient as an attribute for the classification of full-waveform airborne laser scanning data in urban areas. ISPRS Journal of Photogrammetry and Remote Sensing 65(5), 423-432.

Anderson, K., 2009. Remote sensing of soil surface properties. Progress in Physical Geography 33(4), 457-473.

Andújar, D., Escolà, A., Rosell-Polo, J.R., Fernández-Quintanilla, C., Dorado, J., 2013. Potential of a terrestrial LiDAR-based system to characterise weed vegetation in maize crops. Computers and Electronics in Agriculture 92, 11-15.

Andújar, D., Ribeiro, Á., Fernández-Quintanilla, C., Dorado, J., 2011. Accuracy and feasibility of optoelectronic sensors for weed mapping in wide row crops. Sensors 11(3), 2304-2318.

Arias-Estévez, M., López-Periago, E., Martínez-Carballo, E., Simal-Gándara, J., Mejuto, J.-C., García-Río, L., 2008. The mobility and degradation of pesticides in soils and the pollution of groundwater resources. Agriculture, Ecosystems & Environment 123(4), 247-260.

Banerjee, A., Merugu, S., Dhillon, I.S., Gosh, J., 2005. Clustering with Bregman Divergences. Journal of Machine Learning Research 6, 1705-1749.

Breiman, L., 2001. Random Forests. Machine Learning 45(1), 5-32.

Bundesministerium der Justiz und für Verbraucherschutz, 2012. Gesetz zum Schutz der Kulturpflanzen (PflSchG).

Christensen, S., Søgaard, P., Kudsk, P., Nørremark, M., Lund, I., Nadimi, E.S., Jørgensen, R., 2009. Site-specific weed control technologies. Weed Research 49(3), 233-241.

Cohen, J., 1960. A coefficient of agreement for nominal scales. Educational and Psychological Measurement 20(1), 37-46.

Daughtry, C., Hunt Jr., E., 2008. Mitigating the effects of soil and residue water contents on remotely sensed estimates of crop residue cover. Remote Sensing of Environment 112(4), 1647-1657.

Ducic, V., Hollaus, M., Ullrich, A., Wagner, W., Melzer, T., 2006. 3D vegetation mapping and classification using full-waveform laser scanning. Pulse 1, 211-217.

Ehlert, D., Adamek, R., Horn, H.-J., 2009. Laser rangefinder-based measuring of crop biomass under field conditions. Precision Agriculture 10(5), 395-408.

Fabre, S., Lesaignoux, A., Olioso, A., Briottet, X., 2011. Influence of water content on spectral reflectance of leaves in the 3-15 μm Domain. IEEE Geoscience and Remote Sensing Letters 8(1), 143-147.

Feyaerts, F., van Gool, L., 2001. Multi-spectral vision system for weed detection. Pattern Recognition Letters 22(6), 667-674.

Filin, S., Pfeifer, N., 2005. Neighborhood systems for airborne laser data. Photogrammetric Engineering & Remote Sensing 71(6), 743-755.

Gerhards, R., Oebel, H., 2006. Practical experiences with a system for site-specific weed control in arable crops using real-time image analysis and GPS-controlled patch spraying. Weed Research 46(3), 185-193.

Gerke, M., Xiao, J., 2014. Fusion of airborne laserscanning point clouds and images for supervised and unsupervised scene classification. Journal of Photogrammetry and Remote Sensing 87, 78-92.

Guijarro, M., Pajares, G., Riomoros, I., Herrera, P.J., Burgos-Artizzu, X.P., Ribeiro, A., 2011. Automatic segmentation of relevant textures in agricultural images. Computers and Electronics in Agriculture 75(1), 75-83.

Hague, T., Tillett, N.D., Wheeler, H., 2006. Automated crop and weed monitoring in widely spaced cereals. Precision Agriculture 7(1), 21-32.

Han, J., Kramber, M., Pei, J. 2012. Data mining: Concepts and techniques, Third Edition ed. Morgan Kaufmann.

Hansen, M., Dubayah, R., DeFries, R., 1996. Classification trees: An alternative to traditional land cover classifiers. International Journal of Remote Sensing 17(5), 1075-1081.

Heege, H.J., 2013. Precision in crop farming. Site specific concepts and sensing methods: applications and results. Springer, Heidelberg.

Hoffmeister, D., Curdt, C., Tilly, N., Bendig, J., 2010. 3D terrestrial laser scanning for field crop modelling, in: Lenz-Wiedemann, V., Bareth, G. (Eds.), Proceedings on the Workshop of Remote Sensing Methods for Change Detection and Process Modelling. Geographisches Institut der Universität zu Köln - Kölner Geographische Arbeiten, Cologne, Germany, 25-30.

Höfle, B., 2014. Radiometric correction of terrestrial LiDAR point cloud data for individual maize plant detection. IEEE Geoscience and Remote Sensing Letters 11(1), 94-98.

Höfle, B., Hollaus, M., 2010. Urban vegetation detection using high density full-waveform airborne lidar data - combination of object-based image and point cloud analysis. International Archives of Photogrammetry, Remote Sensing and Spatial Information Sciences 37 (Part 7B), 281-286.

Höfle, B., Pfeifer, N., 2007. Correction of laser scanning intensity data: Data and model-driven approaches. ISPRS Journal of Photogrammetry and Remote Sensing 62(6), 415-433.

Hosoi, F., Omasa, K., 2009. Estimating vertical plant area density profile and growth parameters of a wheat canopy at different growth stages using three-dimensional portable lidar imaging. ISPRS Journal of Photogrammetry and Remote Sensing 64(2), 151-158.

Jarmer, T., 2013. Spectroscopy and hyperspectral imagery for monitoring summer barley. International Journal of Remote Sensing 34(17), 6067-6078.

Jarmer, T., Vohland, M., Lilienthal, H., Schnug, E., 2008. Estimation of some chemical properties of an agricultural soil by spectroradiometric measurements. Pedosphere 18(2), 163-170.

Jolliffe, I.T., 2002. Principal Component Analysis, second ed. Springer, New York.

Kaasalainen, S., Jaakkola, A., Kaasalainen, M., Krooks, A., Kukko, A., 2011. Analysis of incidence angle and distance effects on terrestrial laser scanner intensity: search for correction methods. Remote Sensing 3(12), 2207-2221.

Koenig, K., Höfle, B., Müller, L., Hämmerle, M., Jarmer, T., Siegmann, B., Lilienthal, H., 2013. Radiometric correction of terrestrial lidar data for mapping of harvest residues density. ISPRS Annals of the Photogrammetry, Remote Sensing and Spatial Information Sciences 2 (5/W2), 133-138.

Lamb, D.W., Brown, R.B., 2001. Precision agriculture: remote-sensing and mapping of weeds in crops. Journal of Agricultural Engineering Research 78(2), 117-125.

Lilienthal, H., Richter, N., Schnug, E., 2012. Penta-Spek Ein mobiles bodengestütztes hyperspektrales Aufnahmesystem für die Landwirtschaft. Berichte aus der Geoinformatik, 351 - 358.

Lilienthal, H., Schnug, E., 2010. Bodengestützte Erfassung räumlich hochaufgelöster Hyperspektraldaten. Bornimer agrartechnische Berichte 73, 86 - 93.

Lindberg, E., Holmgren, J., Olofsson, K., Wallerman, J., Olsson, H., 2013. Estimation of tree lists from airborne laser scanning using tree model clustering and k-MSN imputation. Remote Sensing 5(4), 1932-1955.

Llorens, J., Gil, E., Llop, J., Queraltó, M., 2011. Georeferenced lidar 3D vine plantation map generation. Sensors 11(6), 6237-6256.

López-Granados, F., 2011. Weed detection for site-specific weed management: mapping and real-time approaches. Weed Research 51(1), 1-11.

Lumme, J., Karjalainen, M., Kaartinen, H., Kukko, H., Hyyppä, J., Hyyppä, H., Jaakola, A., Kleemola, J., 2008. Terrestrial laser scanning of agricultural crops, The International Archives of the Photogrammetry, Remote Sensing and Spatial Information Sciences 37 (Part B5), 563-566.

McCarthy, C.L., Hancock, N.H., Raine, S.R., 2010. Applied machine vision of plants: a review with implications for field deployment in automated farming operations. Intelligent Service Robotics 3(4), 209-217.

Meron, M., Tsipris, J., Orlov, V., Alchanatis, V., Cohen, Y., 2010. Crop water stress mapping for site-specific irrigation by thermal imagery and artificial reference surfaces. Precision Agriculture 11(2), 148-162.

Mulla, D.J., 2013. Twenty five years of remote sensing in precision agriculture: key advances and remaining knowledge gaps. Biosystems Engineering 114(4), 358-371.

Pal, M., Mather, P.M., 2003. An assessment of the effectiveness of decision tree methods for land cover classification. Remote Sensing of Environment 86(4), 554-565.

Palacios-Orueta, A., Ustin, S.L., 1998. Remote sensing of soil properties in the Santa Monica Mountains I. Spectral analysis. Remote Sensing of Environment 65(2), 170-183.

Pearson, K., 1895. Note on regression and inheritance in the case of two parents. Proceedings of the Royal Society of London, 58(347-352), 240-242.

Peña, J.M., Torres-Sánchez, J., de Castro, A., Kelly, M., López-Granados, F., 2013. Weed mapping in early-season maize fields using object-based analysis of unmanned aerial vehicle (UAV) images PLoS ONE 8(10), e77151.

Pérez, A.J., López, F., Benlloch, J.V., Christensen, S., 2000. Colour and shape analysis techniques for weed detection in cereal fields. Computers and Electronics in Agriculture 25(3), 197-212.

Peteinatos, G.G., Weis, M., Andújar, D., Rueda Ayala, V., Gerhards, R., 2014. Potential use of ground-based sensor technologies for weed detection. Pest Management Science 70(2), 190-199.

Pfeifer, N., Höfle, B., Briese, C., Rutzinger, M., Haring, A., 2008. Analysis of the backscattered energy in terrestrial laser scanning data. International Archives of Photogrammetry Remote Sensing and Spatial Information Sciences 37 (Part B5), 1045-1052.

Primicerio, J., Di Gennaro, S., Fiorillo, E., Genesio, L., Lugato, E., Matese, A., Vaccari, F., 2012. A flexible unmanned aerial vehicle for precision agriculture. Precision Agriculture 13(4), 517-523.

Quinlan, J.R., 1986. Induction of Decision Trees. Machine Learning 1(1), 81-106.

Riegl, 2013. Datasheet VZ-400. http://www.riegl.com (Accessed 13 January, 2014)

Romeo, J., Guerrero, J., Montalvo, M., Emmi, L., Guijarro, M., Gonzalez-de-Santos, P., Pajares, G., 2013. Camera sensor arrangement for crop/weed detection accuracy in agronomic images. Sensors 13(4), 4348-4366.

Rosell, J.R., Sanz, R., 2012. A review of methods and applications of the geometric characterization of tree crops in agricultural activities. Computers and Electronics in Agriculture 81, 124-141.

Rosell, J.R., Llorens, J., Sanz, R., Arnó, J., Ribes-Dasi, M., Masip, J., Escolà, A., Camp, F., Solanelles, F., Gràcia, F., Gil, E., Val, L., Planas, S., Palacín, J., 2009. Obtaining the three-dimensional structure of tree orchards from remote 2D terrestrial lidar scanning. Agricultural and Forest Meteorology 149(9), 1505-1515.Rousseeuw, P.J., 1987. Silhouettes: A graphical aid to the interpretation and validation of cluster analysis. Journal of Computational and Applied Mathematics 20, 53-65.

Rumpf, T., Römer, C., Weis, M., Sökefeld, M., Gerhards, R., Plümer, L., 2012. Sequential support vector machine classification for small-grain weed species discrimination with special regard to Cirsium arvense and Galium aparine. Computers and Electronics in Agriculture 80, 89-96.

Rutzinger, M., Höfle, B., Hollaus, M., Pfeifer, N., 2008. Object-based point cloud analysis of full-waveform airborne laser scanning data for urban vegetation classification. Sensors 8(8), 4505-4528.

Saeys, W., Lenaerts, B., Craessaerts, G., De Baerdemaeker, J., 2009. Estimation of the crop density of small grains using lidar sensors. Biosystems Engineering 102(1), 22-30.

Sanz-Cortiella, R., Llorens-Calveras, J., Escolà, A., Arnó-Satorra, J., Ribes-Dasi, M., Masip-Vilalta, J., Camp, F., Gràcia-Aguilá, F., Solanelles-Batlle, F., Planas-DeMartí, S., Pallejà-Cabré, T., Palacin-Roca, J., Gregorio-Lopez, E., Del-Moral-Martínez, I., Rosell-Polo, J.R., 2011. Innovative lidar 3D dynamic measurement system to estimate fruit-tree leaf area. Sensors 11(6), 5769-5791.

Sena Jr., D.G., Costa, M.M., Ragagnin, V.A., Gobbi, K.F.C., Pinto, F., Oliveira Neto, O.V., 2011. Image processing to assess the spatial variability of weeds in no-tillage. Bioscience Journal 27(4), 536-543.

Smith, R.G., Ryan, M.R., Menalled, F.D., 2011. Direct and indirect impacts of weed management practices on soil quality, in: Hatfield, J.L., Sauer, T.J. (Eds.), Soil Management: Building a Stable Base for Agriculture. Soil Science Society of America, pp. 275-286.

Streck, N.A., Rundquist, D., Connot, J., 2002. Estimating residual wheat dry matter from remote sensing measurements. Photogrammetric Engineering & Remote Sensing 68, 1193-1201.

Tellaeche, A., Pajares, G., Burgos-Artizzu, X.P., Ribeiro, A., 2011. A computer vision approach for weeds identification through Support Vector Machines. Applied Soft Computing 11(1), 908-915.

Thorp, K.R., Tian, L.F., 2004. A review on remote sensing of weeds in agriculture. Precision Agriculture 5, 477-508.

Tilly, N., Hoffmeister, D., Cao, Q., Huang, S., Lenz-Wiedemann, V., Miao, Y., Bareth, G., 2014. Multitemporal crop surface models: accurate plant height measurement

and biomass estimation with terrestrial laser scanning in paddy rice. Journal of Applied Remote Sensing 8(1), 083671-01 - 083671-22.

Torres-Sánchez, J., López-Granados, F., De Castro, A.I., Peña-Barragán, J.M., 2013. Configuration and specifications of an unmanned aerial vehicle (UAV) for early site specific weed management. PLoS ONE 8(3), e58210.

Vauhkonen, J., Ene, L., Gupta, S., Heinzel, J., Holmgren, J., Pitkänen, J., Solberg, S., Wang, Y., Weinacker, H., Hauglin, K.M., Lien, V., Packalén, P., Gobakken, T., Koch, B., Næsset, E., Tokola, T., Maltamo, M., 2012. Comparative testing of single-tree detection algorithms under different types of forest. Forestry 85(1), 27-40.

Vibhute, A.D., Gawali, B.W., 2013. Analysis and modeling of agricultural land use using remote sensing and geographic information system: a review. International Journal of Engineering Research and Applications 3(3), 81-91.

Wagner, W., 2010. Radiometric calibration of small-footprint full-waveform airborne laser scanner measurements: Basic physical concepts. ISPRS Journal of Photogrammetry and Remote Sensing 65(6), 505-513.

Weis, M., Gutjahr, C., Rueda Ayala, V., Gerhards, R., Ritter, C., Schölderle, F., 2008. Precision farming for weed management: techniques. Gesunde Pflanzen 60(4), 171-181.

Weis, M., Gerhards, R., 2007. Feature extraction for the identification of weed species in digital images for the purpose of site-specific weed control. Wageningen Academic Publishers, Wageningen, 537-544.Westoby, M.J., Brasington, J., Glasser, N.F., Hambrey, M.J., Reynolds, J.M., 2012. 'Structure-from-Motion' photogrammetry: a low-cost, effective tool for geoscience applications. Geomorphology 179, 300-314.

Whiting, M.L., Li, L., Ustin, S.L., 2004. Predicting water content using Gaussian model on soil spectra. Remote Sensing of Environment 89(4), 535-552.

Zhang, C., Kovacs, J., 2012. The application of small unmanned aerial systems for precision agriculture: a review. Precision Agriculture 13(6), 693-712.

Zhang, H., 2004. The Optimality of Naive Bayes, in: Barr, V., Markov, Z. (Eds.), Proceedings of the Seventeenth International Florida Artificial Intelligence Research Society Conference FLAIRS 2004. AAAI Press.

Zhang, L., Grift, T.E., 2012. A LIDAR-based crop height measurement system for Miscanthus giganteus. Computers and Electronics in Agriculture 85, 70-76.

Zimdahl, R.L., 2013. Harmful aspects of weeds, The Fundamentals of Weed Science, 4 ed. Academcic Press Elsevier, 35-35.

Zlinszky, A., Mücke, W., Lehner, H., Briese, C., Pfeifer, N., 2012. Categorizing Wetland Vegetation by Airborne Laser Scanning on Lake Balaton and Kis-Balaton, Hungary. Remote Sensing 4(12), 1617-1650.